Oxygen transport properties of tubular Ce0.9Gd0.1O1.95-La0.6Sr0.4FeO3d composite asymmetric oxygen permeation membranes supported on magnesium oxide

Ovtar, Simona; Gurauskis, Jonas; Bjørnetun Haugen, Astri; Chatzichristodoulou, Christodoulos; Kaiser, Andreas; Hendriksen, Peter Vang

Published in:
Journal of Membrane Science

Link to article, DOI:
10.1016/j.memsci.2016.09.060

Publication date:
2017

Document Version
Peer reviewed version

Oxygen transport properties of tubular $Ce_{0.9}Gd_{0.1}O_{1.95}$-$La_{0.6}Sr_{0.4}FeO_{3-d}$ composite asymmetric oxygen permeation membranes supported on magnesium oxide

Simona Ovtar[a,*], Jonas Gurauskis[a,1], Astri Bjørnetun Haugen[a], Christodoulos Chatzichristodoulou[a], Andreas Kaiser[a], Peter Vang Hendriksen[a]

[a] Department of Energy Conversion and Storage, Technical University of Denmark, Frederiksborgvej 399, DK-4000 Roskilde, Denmark

* Corresponding author

E-mail addresses: simov@dtu.dk (S. Ovtar), jonasg@aeneam.com (J. Gurauskis), ahua@dtu.dk (A. Bjørnetun Haugen), ccha@dtu.dk (C. Chatzichristodoulou), akai@dtu.dk (A. Kaiser), pvhe@dtu.dk (P. V. Hendriksen)

Abstract

The oxygen permeation through dense $Ce_{0.9}Gd_{0.1}O_{1.95}$ – $(La_{0.6}Sr_{0.4})_{0.98}FeO_{3-d}$ dual-phase composite asymmetric membranes supported on a porous MgO tube was studied. The membranes were prepared by thermoplastic extrusion, dip coating, co-sintering and infiltration of a catalyst. Oxygen permeation measurements and electrical conductivity characterization of the membrane were performed as a function of temperature and oxygen partial pressure. The oxygen flux through the membrane in a H_2/air gradient at 850 °C reached 15 N ml cm^{-2} min^{-1}. The measured oxygen flux was in good agreement with the theoretically estimated one, taking into account the transport properties of the composite, surface exchange losses, gas diffusion and gas conversion in the MgO support. The performance of the membrane was limited by the surface exchange for the operation in N_2/air, CO_2/air and H_2/air at low temperatures and most probably by the porosity of the MgO support for the operation in H_2/air at 850 °C. The stability tests of the membrane in CO_2/air and H_2/air configurations revealed that an initial degradation of the oxygen flux occurs and it is followed by a relatively stable performance. Post-mortem analysis of the membrane after 900 h of operation did not reveal any significant microstructural degradation of the membrane layer.

Keywords: oxygen permeation membrane, dual-phase composite, asymmetric membrane, oxygen flux, electrical conductivity relaxation

[1] Current address: Æneam ApS, Denmark.

Highlights:

1. The performance of the oxygen permeation membrane was stable in CO_2 and H_2.

2. The maximal oxygen flux was 15 N ml cm^{-2} min^{-1} at 850 °C in the H_2/air configuration.

3. For most of testing conditions the oxygen flux was limited by surface exchange.

4. The maximal oxygen flux was most probably limited by porosity of the MgO support.

5. The measured oxygen flux was well in agreement with the theoretically predicted one.

Graphical abstract

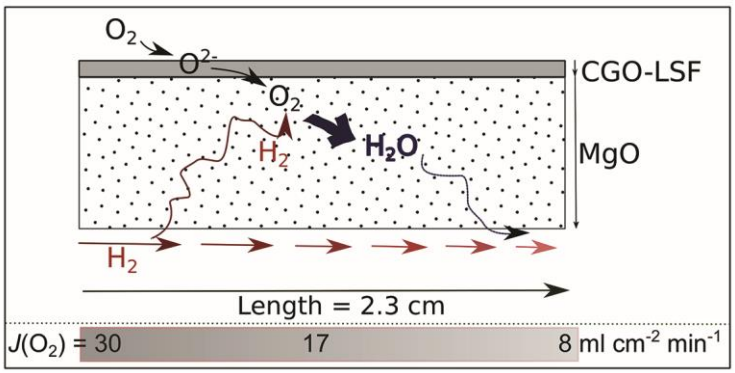

1 Introduction

Mixed ionic electronic conducting (MIEC) perovskites with the composition $A_xSr_{1-x}Fe_yB_{1-y}O_{3-\delta}$ have been intensively investigated for application in high temperature oxygen transport membranes (OTM). OTMs can be employed in reactors for oxygen separation, partial oxidation of hydrocarbons, production of syngas, C-C coupling, etc. [1–3].

Among the MIEC perovskites, $Ba_xSr_{1-x}Fe_yCo_{1-y}O_{3-\delta}$ (BSCF) has attracted great attention due to its high ionic and electronic conductivity and its fair stability under certain application conditions (high temperature, high oxygen partial pressure). Different modules with planar and tubular membranes of BSCF have been manufactured and tested [3–6]. The highest oxygen flux of 12.2 ml cm^{-2} min^{-1} for 70 μm thick planar asymmetric BSCF membranes at 1000 °C for air/Ar was reported by Bauman et al. [6].

A major limitation of many of the fast transport MIEC perovskites is the thermodynamic instability at low oxygen partial pressures. Cobalt-containing perovskites (like BSCF, $La_xSr_{1-x}CoO_{3-\delta}$ and $La_xSr_{1-x}Fe_yCo_{1-y}O_{3-\delta}$) are considered for applications with a pO_2 as low as 101.3 Pa (10^{-3} atm). At lower pO_2's these perovskites start to

decompose, for example $La_{0.6}Sr_{0.4}Fe_yCo_{1-y}O_{3-\delta}$ (y = 0.2, 0.4) was found to decompose into A_2BO_4 and CoO at pO_2 of 0.101 Pa (10^{-6} atm) at 800 °C [7]. Much better stability down to a pO_2 of approx. 10^{-14} Pa has been shown for the chromium ($La_xA_{1-x}Cr_yB_{1-y}O_{3-\delta}$) [8] and iron ($La_xSr_{1-x}FeO_{3-\delta}$) based perovskites [9], but the disadvantage of these materials is a low ionic conductivity, especially at low temperatures, as presented in Table 1. Therefore, a relatively low oxygen permeation flux of 1.54 N ml cm^{-2} min^{-1} at 900 °C for a pO_2 gradient of 2.13 x 10^4 Pa /5 x 10^{-11} Pa for a 1.34 mm thick $(La_{0.6}Sr_{0.4})_{0.99}FeO_{3-\delta}$ pellet was reported by Søgaard et al. [10].

Table 1: Reported ionic conductivities (σ_i) of MIEC materials commonly used for oxygen permeation membranes

Materials	σ_i @ 700 °C [S cm^{-1}]	σ_i @ 900 °C [S cm^{-1}]	Ref.
$La_{0.6}Sr_{0.4}FeO_{3-d}$	0.002	0.049	[10]
$La_{0.8}Sr_{0.2}Cr_{0.5}Fe_{0.5}O_{3-d}$	/	0.01 @ 950 °C	[8]
$La_{0.6}Sr_{0.4}Fe_{0.8}Co_{0.2}O_{3-d}$	0.013	0.09	[11]
$Ba_{0.5}Sr_{0.5}Co_{0.8}Fe_{0.2}O_{3-d}$	0.25	0.96 @ 800 °C	[12]
$Ce_{0.9}Gd_{0.1}O_{2-d}$	0.03	0.12	[13]

Another important requirement for using the OTM in partial oxidation of hydrocarbons or syngas production or in oxyfuel schemes involving a flue gas sweep is the thermodynamic stability in CO_2. Most barium and strontium containing perovskites form thermodynamically stable carbonates [14] with CO_2 at OTM operating temperatures (700 – 900 °C), which can strongly reduce the oxygen surface exchange kinetic and especially for thin membranes significantly reduce the achievable fluxes.

Doped ceria may offer an alternative as it shows high oxide ion conductivity (Table 1) and high thermodynamic stability in various gases (e.g. SO_2, CO_2), but it is limited by low electronic conductivity under oxidizing conditions. The p-type electronic conductivity of CGO in air at 900 °C is 6.5 x 10^{-4} S cm^{-1} and the n-type electronic conductivity becomes significant only at highly reducing conditions below a pO_2 of 10^{-9} Pa. Therefore, a relatively low oxygen permeation flux of 7 x 10^{-5} ml cm^{-2} min^{-1} was measured for a 1.35 mm thick

CGO membrane at 950 °C for an Air/Ar configuration [15]. The performance of CGO membranes can be improved by increasing the electronic conductivity of CGO at high oxygen partial pressures using mixed valence dopants [16]. Mixed valence elements like Pr or Tb introduces p-type conductivity to ceria [17]. Donor doping with Nb_2O_5 or WO_3 enhances n-type conductivity in CGO at intermediate pO_2 (10^{-5} – 10^4 Pa) [18].

Additionally, the oxygen permeation flux can be drastically increased by reducing the thickness of the membrane and introducing suitable catalyst layer for the oxygen reduction/oxidation reaction. This was shown for a 30 μm thin CGO layer supported on an YSZ/Ni porous support with a Ni-YSZ and LSCF-CGO electro-catalyst layers by Chatzichristodoulou et al. [19]. For this membrane assembly, the oxygen permeation flux reached 16 N ml cm^{-2} min^{-1} at 900 °C for an air/steam-H_2 configuration.

Alternatively, composites of a good ionic and a good electronic conductor can simultaneously meet the requirements for chemical stability and good transport properties [20]. The oxygen permeation fluxes of different thin asymmetric dual phase composite membranes reported in the literature are summarized in Table 2.

Table 2: Oxygen permeation flux of thin asymmetric dual phase composite membranes

Membrane	Support	J_{O2} ml cm^{-2} min^{-1}	T °C	Thickness μm	Catalyst	pO_2'/pO_2''	Ref.
$La_{0.6}Sr_{0.4}FeO_{3-d}$/ $Ce_{0.9}Gd_{0.1}O_{1.95}$	LSF/CGO	1.41	900	100	$La_{0.6}Sr_{0.4}CoO_{3-d}$	Air/He	[21]
$La_{0.6}Sr_{0.4}Co_{0.2}Fe_{0.8}O_{3-d}$ + $Ce_{0.8}Tb_{0.2}O_{2-d}$/ $NiFe_2O_4$	LSCF	4.8	1000	10 + 8	/	Air/Ar	[22]
$La_{0.8}Sr_{0.2}Cr_{0.5}Fe_{0.5}O_{3-d}$/ $Zr_{0.8}Y_{0.2}O_{2-d}$	YSZ	0.06 1.2	900	120	/	Air/Ar Air/CO	[23]
$Bi_{1.5}Y_{0.3}Sm_{0.2}O_3$/ $La_{0.8}Sr_{0.2}MnO_{3-d}$	BYS/LSM	0.5	850	290	/	Air/He	[24]

$Sm_{0.6}Sr_{0.4}FeO_{3-d}$/ $Ce_{0.85}Sm_{0.15}O_{1.925}$	SSF/CSO	1	950	160	$La_{0.6}Sr_{0.4}CoO_{3-d}$	Air/He	[25]
$Sm_{0.6}Sr_{0.4}Al_{0.3}Fe_{0.7}O_{3-d}$/ $Ce_{0.85}Sm_{0.15}O_{1.925}$	SMAF/CSO	3.9	950	40	$Sm_{0.5}Sr_{0.5}CoO_{3-d}$	Air/He	[26]
$(La_{0.6}Sr_{0.4})_{0.98}FeO_{3-d}$/ $Ce_{0.9}Gd_{0.1}O_{1.95}$	MgO	2.1 15	850	10	$LaCoO_{3-d}$	Air/N_2 Air/H_2	this study

The CGO-LSF composite reported in this study was selected based on the requirements of thermodynamic stability over a broad pO_2 range and its high performance reported in previous studies. Samson et al. [9] reported an oxygen flux of 0.12 ml cm^{-2} min^{-1} at 800 °C for air/N_2 configuration of a 1 mm thick pellet of a 50 vol.% $Ce_{0.9}Gd_{0.1}O_{1.95}$ / 50 vol.% $La_{0.6}Sr_{0.4}FeO_{3-d}$ composite coated with a $La_{0.6}Sr_{0.4}CoO_{3-d}$ electro-catalyst layer. A much higher oxygen flux of 1.41 ml cm^{-2} min^{-1} for a planar thin asymmetrical membrane of 70 vol.% $Ce_{0.9}Gd_{0.1}O_{1.95}$ / 30 vol.% $La_{0.6}Sr_{0.4}FeO_{3-d}$ composite was reported by Cheng et al. [21] (Table 2).

The aim of this work was to study the temperature and pO_2 dependence of the transport properties and oxygen permeation flux of the dual phase $Ce_{0.9}Gd_{0.1}O_{1.95}$ - $(La_{0.6}Sr_{0.4})_{0.98}FeO_{3-d}$ composite membrane as well as its stability over hundreds of hours. The membrane was in the form of a thin membrane layer on top of a thick porous support that provided the necessary mechanical strength. For the support a low coast construction type ceramic, MgO, was used. Furthermore, the oxygen flux through the membrane was theoretically estimated, taking into account the electronic and ionic conductivity of the membrane material, the surface exchange reaction on the feed and the permeate side, the gas concentration polarization, and the gas conversion. These estimates gave a useful insight to the processes–limiting performance under operating conditions.

2 Experimental

2.1 Materials

Fine MgO powder (product 12R-0801, surface area >20 m^2/g) for the porous, tubular support was supplied by Inframat Corporation (USA). The MgO powder was calcined at 1000 °C for 10 h to reduce the surface area to 10.5 m^2/g. Graphite (Timrex KS6, d_{50} 3.4 µm) from Imerys Graphite & Carbon (Switzerland) was used as a sacrificial pore former in the support. Three polymers were used to form a thermoplastic feedstock for the

extrusion: ethylene-vinyl acetate copolymer resin (Elvax® 250) from Du Pont (USA), stearic acid and paraffin wax, both from Sigma Aldrich (USA).

Two different surface area gadolinium doped cerium oxide ($Ce_{0.9}Gd_{0.1}O_{1.95}$, CGO) powders were supplied by Rhodia (France). A CGO powder with a specific surface area of 7 m^2/g (further denoted as CGO-ul) was used in the dense dual phase membrane layer, whereas a CGO powder with a specific surface area of 35.5 m^2/g (further denoted as CGO-uh) was used in the porous catalyst layers. The lanthanum strontium ferrite ($(La_{0.6}Sr_{0.4})_{0.98}FeO_{3-d}$, LSF) used as the electronic conducting phase within the dense dual phase membrane was supplied by Mitsuya Boeki Ltd. (Japan). The CGO-ul and LSF powders were used in the as received state, whereas the CGO-uh powder was pre-calcined at 1100 °C (dwell 2 h). The specific surface area after calcination was 1.72 m^2/g. Low molecular weight (Mw=10000 g/mol) polyvinylpyrolidone (PVP K15, Sigma Aldrich) was used as a surfactant. Higher molecular weight (Mw=30000-70000 g/mol) polyvinyl butyral (B-98, Butvar) and polyvinylpyrolidone (PVP K30, Sigma Aldrich) were used as binders. Reagent grade ethanol from Sigma-Aldrich was used as the solvent carrier for the colloidal suspension. Dibutyl sebacate (DBS, Sigma Aldrich) was used as plasticizer. Graphite powder, used as sacrificial pore former in the catalyst layers, with particle size of d_{V50}= 4-5 µm was supplied by Graphit Kropfmühl (Germany).

2.2 Thermoplastic extrusion

The calcined MgO powder was coated with stearic acid (0.063 g stearic acid per 1 g MgO) to reduce the dust formation and improve the adhesion to the thermoplastic polymers by mixing MgO and stearic acid in 1-propanol (Sigma Aldrich) for 24 hours, and then evaporating the 1-propanol. A thermoplastic feedstock was obtained by compounding the coated MgO powder (43 vol%), the thermoplastic binders (25.8 vol% Elvax and 11.4 vol% paraffin vax) and graphite (20.2 vol%) at 110-115 °C for 2 h in a kneader (Model BK20, Hermann Linden, Germany). The thermoplastic feedstock was shaped into tubes (14 mm outer diameter, 12 mm inner diameter) using a screw extruder (Model 19/20DN, Brabender, Germany) operating at 110 °C. A more detailed description of the thermoplastic extrusion of porous MgO tubes can be found elsewhere [27].

2.3 Dip coating, sintering and infiltration

Table 3. Composition of suspensions used for deposition of functional layers.

	Suspensions

		Dense CGO-LSF	Porous CGO
Proportion of solid phases (vol.%)	CGO-ul	70	--
	CGO-uh	--	60
	LSF	30	--
	Graphite	--	40
Final composition (vol.%)	Solid loading	5	7
	Solvent	90.5	86.6
	Surfactant	3	--
	Binder PVP	1.5	1
	Binder PVB	--	3
	Plasticizer DBS	--	2.4

The membranes' functional layers were deposited by dip coating onto the MgO supports prepared by thermoplastic extrusion. The dip coating suspensions were prepared by ball-milling the constituents in polystyrene bottles with zirconia balls. All the constituents of the dense CGO/LSF suspension were milled together for 48 h. In the case of porous CGO suspension an initial ball milling for 24 h was done for all the constituents except graphite. After the addition of graphite, the suspension was further milled for 30 min. Detailed compositions of suspensions used in this study are given in Table 3.

Three different layers were applied on the MgO structural support: a porous CGO active layer, a dense dual phase membrane layer and a porous CGO active layer on the outer side of membrane. Thermal treatments were applied in between the different coatings, with a final sintering step at 1250 °C for 2h. A more detailed description of the dip coating and co-sintering process can be found elsewhere [28].

The outer porous CGO active layer was infiltrated with a precursor solution of a catalyst. A methanol solution of Co nitrate (30 mmol/g) and La nitrate (30 mmol/g) with a molar ratio La:Co = 1:1 was prepared. The infiltration was done by applying the precursor solution with a brush and performing a heat treatment at 350 °C for 30 min. The infiltration process was repeated three times to increase the load of the catalyst in the porous layer. The catalyst $LaCoO_{3-d}$ was chosen due to reported good performance as an oxygen electrode [29] and to avoid alkaline earth metals.

2.4 Microstructural characterization

Polished and fractured cross sections before and after permeation testing of the tubular membrane were analyzed using a Hitachi TM300 and a Zeiss SUPRA scanning electron microscope.

The open porosity and the pore neck size were determined by Hg porosimetry (Poremaster© GT, Quantachrome Instruments, USA).

2.5 Electrical conductivity measurements

The powders of CGO (CGO-ul) and LSF were mixed together and ball milled for 24 h in ethanol. The volume fraction of CGO in LSF was varied from 0 vol.% to 95 vol.%. Rectangular bars were formed from the composite powders by uniaxial pressing at 3 MPa and further isostatic pressure of 325 MPa. The bars were sintered at 1300 °C for 2h to a density higher than 95 % of the theoretical density. The sintered bars were polished down to a surface roughness of 1 μm and a final geometry of ca. 2 x 2 x 20 mm.

The electrical conductivity was measured using 4-point measurements. A current of 10 mA was applied through the sample and the voltage drop was measured over a well-defined distance in the center of the sample. The sample was placed in a quartz tube, where the atmosphere can be changed within < 10 s. The composites with 70 vol.% of CGO and 30 vol.% of LSF were characterized in two pO_2 ranges: i) 1.0 x 10^5 Pa – 1.0 Pa with varying the flow rates ratio of N_2 and O_2 and ii) 10^{-3}-10^{-19} Pa with varying the flow rates ratio of CO_2 and CO. For pre-mixing the gases a four-way valve system (Brooks) was used. The total flow rate of gases was fixed to 12 l/h. The studied temperature range was 650 - 900 °C. A more detailed description of the experimental setup is reported elsewhere [30,31].

2.6 Electrical conductivity relaxation measurements

At high pO_2 (1.0 x 10^5 Pa – 1.0 Pa) electrical conductivity relaxation (ECR) was carried out on i) a piece of the tubular CGO-LSF composite membrane supported on the porous MgO with the CGO active layer and ii) an LCO infiltrated piece of the same membrane. The measurements were carried out upon increasing pO_2 by a factor of 2 ($pO_{2(start)} = \frac{1}{2} \bullet pO_{2(end)}$), to simulate oxygen uptake at the surface of the membrane. At low pO_2 (10^{-3} – 10^{-19} Pa) the ECR was measured on i) a dense dual phase composite CGO-LSF (bar) and ii) a piece of the membrane without LCO infiltration. The measurements were carried out upon decreasing pO_2 by a factor of 10 ($pO_{2(start)} = 10 \bullet pO_{2(end)}$), to simulate the oxygen release.

Fick's second law of diffusion with a first order surface exchange reaction was fitted to the recorded electrical conductivity relaxation curves. This method is well described in the literature for obtaining the oxygen transport properties, which are the surface exchange coefficient (k_{ex}) and the chemical diffusion coefficient (D_{chem}) of oxygen [10,32]. The method of least square fit that calculates the sum of the squared deviation (SSD) between all fitted and measured data points for a k_{ex} and D_{chem} couple was used to derive the k_{ex} and D_{chem} values from relaxation curve. The lowest sum of the squared deviation (SSD_{min}) represented the transient and corresponding k_{ex} and D_{chem} couple that agrees best with measured data [32]. The errors of derived values were estimated by fixing one of the coefficients and varying the other one and were in the range of SSD_{min} ± 5% for k_{ex} and SSD_{min}± 1% for D_{chem}. For the CGO-LSF (bar) at low pO_2 mixed control of k_{ex} and D_{chem} was assumed and the values were derived by Eq. 1[10,32]. For the membranes, which are thin, a surface exchange limitation was assumed and the relaxation curves were fitted by Eq. 2, as is reported by Søgaard [33].

$$\frac{\sigma_\infty - \sigma(t)}{\sigma_\infty - \sigma(t_0)} = \sum_{n=1}^{\infty} \frac{2L_x^2 \exp\left(\frac{-\beta_{n,x}^2 D_{chem} t}{l_x^{\,2}}\right)}{\beta_{n,x}^2\left(\beta_{n,x}^2 + L_x^2 + L_x\right)} \sum_{n=1}^{\infty} \frac{2L_y^2 \exp\left(\frac{-\beta_{n,y}^2 D_{chem} t}{l_y^{\,2}}\right)}{\beta_{n,y}^2\left(\beta_{n,y}^2 + L_y^2 + L_y\right)}, \quad \beta_{n,x,y}^2 \tan \beta_{n,x,y}^2 = L_{xy} \quad , L_{xy} = \frac{l_{xy} k_{ex}}{D_{chem}} \quad \text{Eq. 1}$$

$$\frac{\sigma_\infty - \sigma(t)}{\sigma_\infty - \sigma(t_0)} = \exp\left(-\frac{k_{ex} t\left(l_x + l_y\right)}{l_x\, l_y}\right) \text{Eq. 2}$$

$\sigma(\infty)$ is the conductivity at steady state after a step change in pO_2, $\sigma(t)$ is the conductivity at the time t during the relaxation and $\sigma(t_0)$ is the conductivity before the step change in pO_2. $2l_x$ and $2l_y$ are the edges of the cross section of the sample. For accurate ECR results the sample dimensions should fulfill the criteria of $l_x \approx l_y << l_z$, where z is the direction of the electronic current. A two-dimensional solution of the diffusion problem was used because the conductivity was measured over a short distance close to the center of the sample. For the studied composite additional assumptions were taken: i) the phases are randomly distributed and the composite was treated as an effective medium, ii) at high pO_2 the conductivity change after a pO_2 step reflects only a change of oxygen concentration in the LSF, and iii) at high pO_2 surface exchange occurs only on the LSF surface [30].

The oxygen surface exchange coefficient (k_O), oxygen diffusion coefficient (D_O) and vacancy diffusion coefficient (D_V) were calculated from the experimentally determined quantities, D_{chem} and k_{ex} by Eqs. 3.

$$k_O = \frac{k_{ex}}{\gamma_O}, \quad D_O = \frac{D_{chem}}{\gamma_O}, \quad D_V = \frac{D_{chem}}{\gamma_V} \quad \gamma_O = \frac{1}{2}\frac{\partial \ln pO_2}{\partial \ln C_O}, \quad \gamma_V = \frac{1}{2}\frac{\partial \ln pO_2}{\partial \ln C_V} \quad \text{Eq. 3}$$

γ_O and γ_V are the thermodynamic factors of oxygen and vacancies, respectively. The thermodynamic factors were estimated from the pO_2 dependence of the oxygen vacancy concentration (C_V) of the CGO-LSF composite by treating the composite as an effective medium, taking δ to be the sum of the oxygen non-stoichiometry of CGO and LSF weighted by their respective molar concentration. Defect thermodynamic data for CGO and LSF were taken from Ref. [34] and Ref. [10], respectively.

2.7 Oxygen permeation flux measurements

Permeation experiments were carried out using a 4-end mode setup with the inner side as the permeate side and the outer side of the tube as the feed side. The rig is schematically illustrated in Figure 1. Alumina tubes were used to support the tubular membrane and to supply gas to its interior. The tubular membranes were situated in the hot zone of the furnace and the temperature was monitored by placing thermocouples inside the alumina tubes at the inlet and the outlet of the tubular membrane. The temperature deviation between the two temperatures was small (~5 °C) and therefore in the following, the average temperature is reported. The membranes were sealed on the alumina support using sodium aluminosilicate sealing glass (NAS)[9]. The active membrane area was 9 cm^2, for a membrane length of 2.3 cm and an outer diameter of 1.25 cm. The OTM was tested in three different configurations: i) N_2/air, ii) CO_2/air, and iii) H_2/air. A constant air flow on the feed side (in the range 30 – 120 l/h) and a flow of different gases (N_2, CO_2, H_2 humidified at 25 °C) on the permeate side were supplied (Figure 1). H_2 was humidified to have a well-defined pO_2 in inlet gas and to mitigate the extreme reducing conditions. The gas flow was controlled and measured using mass-flow controllers (Brooks). The oxygen permeation was studied in the temperature range between 700 °C and 900 °C, varying the pO_2 gradient by changing the inlet gas flow. The oxygen partial pressure (pO_2) of the inlet ($pO_{2(in)}$) and the outlet gas ($pO_{2(out)}$) of the permeate stream was measured using an in-house built YSZ-based sensor. Stability tests of the membrane were done in pure CO_2 at 850 °C and humidified hydrogen at 700 °C. The oxygen permeation flux ($J(O_2)$) for the N_2/air and the CO_2/air configuration was calculated by Eq. 4.

$$J(O_2) = \frac{\Phi_{out}\left(pO_{2(out)} - pO_{2(in)}\right)}{p_{tot}A} \quad \text{Eq. 4}$$

Here Φ_{out} is the outlet flow of gases on the permeate side, A is the surface area of the membrane and p_{tot} is the total pressure, which was 1 atm (1.01325 x 10^5 Pa).

For the H_2/air configuration it was assumed that reaction ($H_2(g)+\frac{1}{2}O_2(g)\rightarrow H_2O(g)$) is in equilibrium and can be described with a known equilibrium constant (K_{eq}(T))[35]. The $J(O_2)$ was calculated from the volume flows of the produced water ($\Phi_{H_2O}^{out}-\Phi_{H_2O}^{in}$) by Eq. 5, as is described in more details by Chatzichristodoulou et al.[19].

$$J(O_2)=\frac{\Phi_{H_2O}^{out}-\Phi_{H_2O}^{in}}{2A} \quad \text{Eq. 5}$$

Gas tightness quality was evaluated by comparing the difference between the inlet and the outlet flow rate after high temperature sealing at 980 °C for 1 h. In this study, for an inlet flow of 400 ml/min of N_2 an outlet flow of ca. 408 ml/min was measured at 850 °C. The difference in the inlet and outlet flow corresponded to the flux of oxygen calculated from Eq. 4. Additionally to this, the membrane was slightly pressurized with an inside overpressure corresponding to ca. 200 Pa (2 x 10^{-3} atm). The leak rate was small and below the uncertainty of the measured outlet flow. Therefore, a leak-less membrane could safely be assumed in the following and the data were not corrected for any leakage.

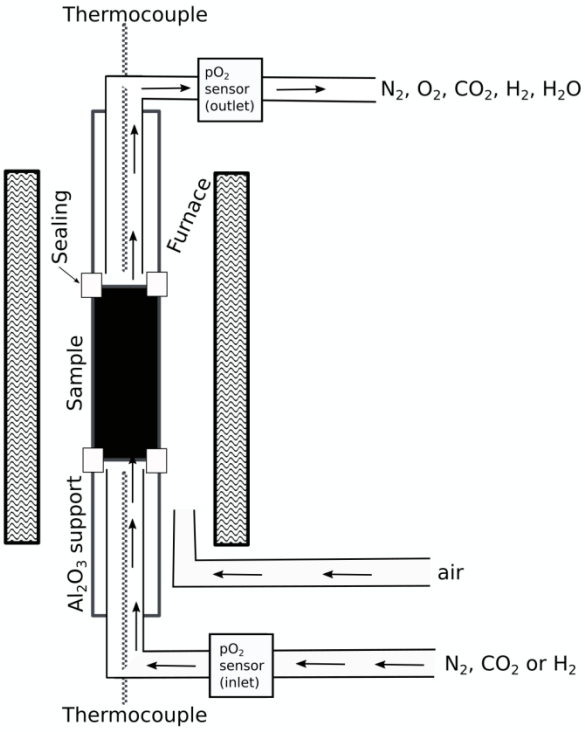

Figure 1: Schematic presentation of the oxygen permeation flux measurement 4-end mode setup for a tubular OTM.

2.8 Modeling the oxygen flux

For the H_2/air configuration the oxygen permeation flux was calculated using a two-dimensional numerical model reported in Ref. [36] that accounts for ambipolar diffusion through the dense membrane, surface exchange at the catalyst layers at the feed and permeate side of the membrane, fuel conversion along the gas flow in the interior of the tubular membrane, and mass transport through the porous MgO support. The numerical model employs Wagner's equation for ambipolar diffusion:

$$J\left(O_2\right) = \frac{RT}{16F^2L}\int_{\ln p(O_2)^*}^{\ln p(O_2)^{**}} \frac{\sigma_{el}\sigma_{ion}}{\sigma_{el}+\sigma_{ion}} d\ln p(O_2) \qquad \text{(Eq. 7)}$$

where R, T and F are the gas constant, the temperature and the Faraday constant, respectively. L is the thickness of the membrane. The effective ionic conductivity (σ_{ion}) was estimated from the Bruggeman-Landauer model [37] for CGO:LSF = 70:30 vol. %. The ionic conductivity of LSF was assumed to be negligible. Literature values from Wang et al.[13] were used for the ionic conductivity of CGO. The electronic conductivity (σ_{el}) was deduced from the measured electrical conductivity of the composite upon subtraction of the effective ionic conductivity of CGO.

The model also takes into account the driving force losses at the catalysts at the feed and permeate side of the membrane, related to the gaseous oxygen reduction and fuel oxidation, respectively, as well as the H_2 conversion and the gas diffusion resistances in the porous support structure at the permeate side. Linear Chang–Jaffe [38] electrode kinetics are employed and the electrode activation polarization resistances (R_{surf}) are assumed to be independent of the gas composition. Mass transport through the porous support structure is described using the dusty gas model with viscous flow. The support thickness was set to 1 mm, having 39 % porosity, 0.47 µm pore size, and tortuosity of 1.5. The thickness of the dense CGO-LSF composite membrane was 10 µm.

3 Results and discussion

3.1 Microstructure of the thin dual phase membrane

A SEM micrograph of a polished cross section of the tubular membrane before permeation test is shown in Figure 2a. The MgO support is approx. 1 mm thick and contains around 39 % of open porosity with a median

pore neck size of 0.47 µm determined by Hg-porosimetry. The thicknesses of the inner porous CGO layer, the dense CGO-LSF composite layer and the porous outer CGO layer are around 10, 10 and 20 µm, respectively (Figure 2b, 2d).

In Figure 2c a fractured cross-section of the porous CGO layer at the feed side is shown. The small particles on the surface of the CGO grains represent the infiltrated LCO catalyst nanoparticles. The average particle size of the infiltrated catalyst before permeation testing of the membrane was 30 ± 5 nm. During the test the LCO particles grew and the final size after more than 900 h of testing at different elevated temperatures and in different configurations was 130 ± 45 nm, as shown in Figure 2e.

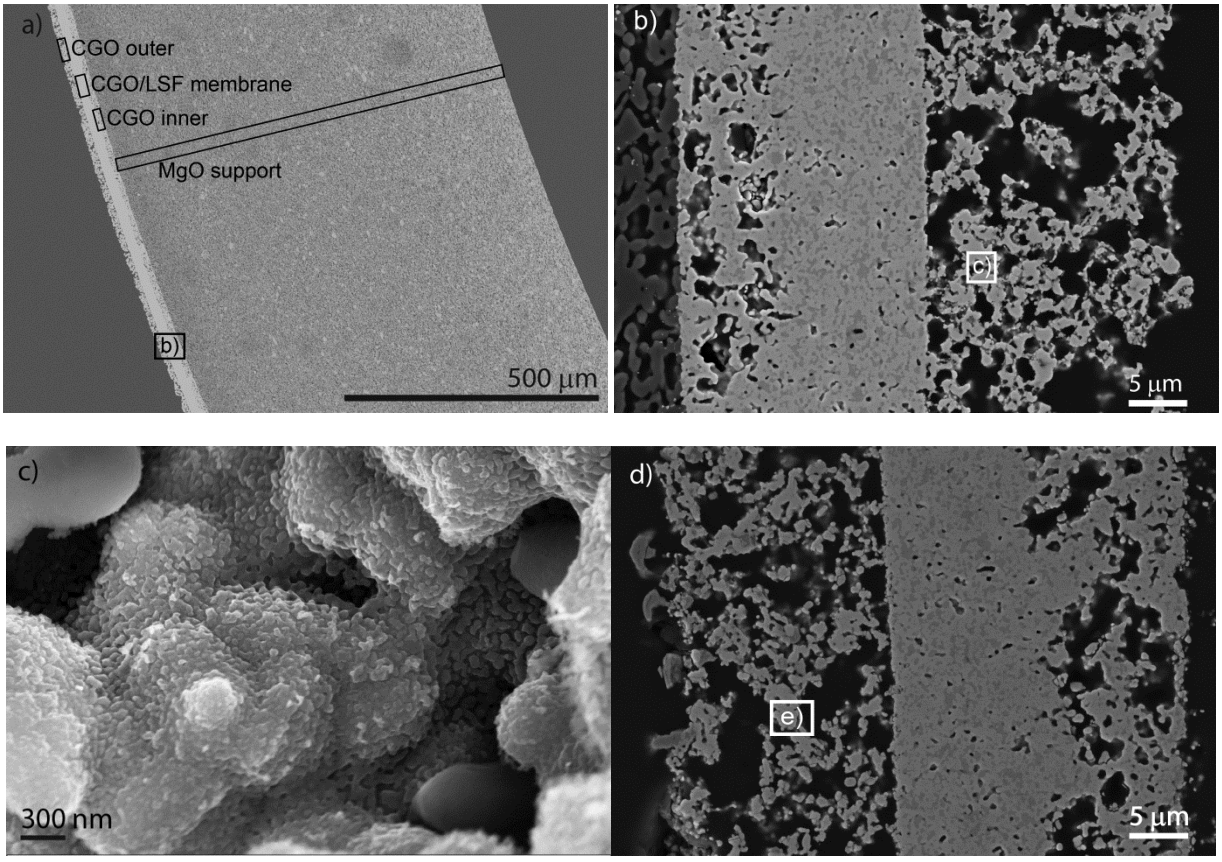

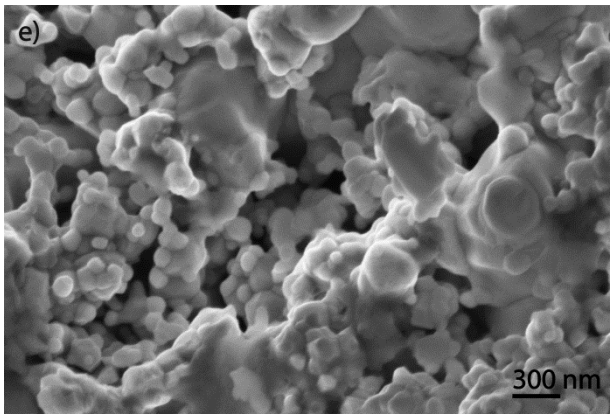

Figure 2: SEM microstructures of a) the membrane supported on the porous MgO support, b) CGO-LSF dual-phase membrane layer with inner and outer porous CGO catalytic layers before testing, c) the infiltrated LCO into the porous CGO layer on the feed side (CGO outer), d) CGO/LSF dual-phase membrane layer with inner and outer porous CGO catalytic layers after testing e) the infiltrated LCO catalyst after membrane operation for more than 900 h.

3.2 Electrical conductivity

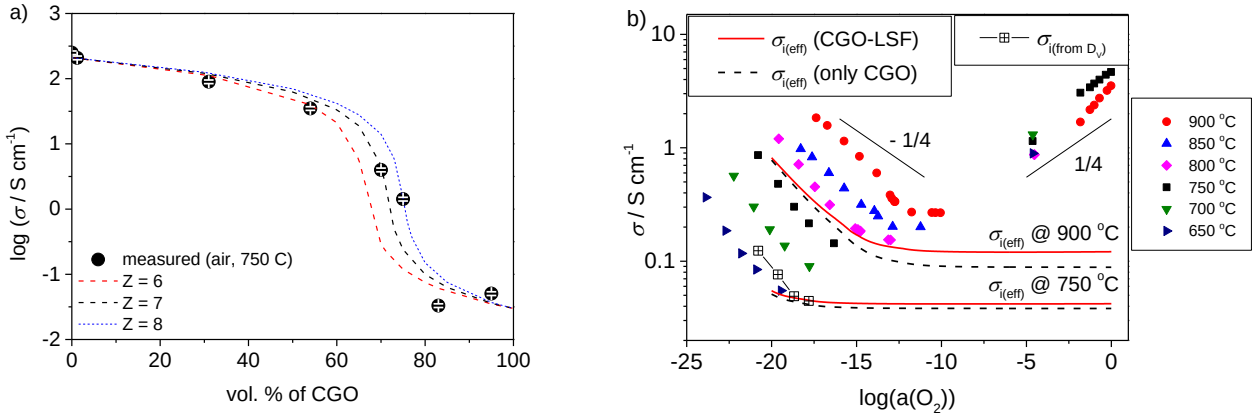

Figure 3: a) Measured electrical conductivities of the CGO-LSF composites for different vol.% of CGO and calculated electrical conductivities for different coordination numbers (Z). b) Electrical conductivity of the CGO-LSF (bar) (70 vol.% of CGO) versus the oxygen activities at different temperatures, the effective ionic conductivity ($\sigma_{i(eff)}$) of the composite for only CGO (dashed) and for CGO-LSF in the composite (solid), and the ionic conductivity calculated from D_V at 750 °C.

Figure 3a shows the electrical conductivity of the dual phase CGO-LSF composites measured in air at 750 °C as a function of the CGO volume fraction (the error bars represent the error derived from measured dimensions of the samples). The electrical conductivity is decreasing with increasing CGO fraction, as it is expected from the lower electrical conductivity of CGO (6.5 x 10^{-2} S cm^{-1} at 750 °C in air) [39] compared to LSF (250 S cm^{-1}). Figure 3a also shows a calculated electrical conductivity for different coordination numbers (Z) of CGO and LSF grains using effective medium percolation theory reported in Ref. [37], where two assumptions for the MIEC phases were made: i) randomly distribution of phases, and ii) grain sizes are smaller than sample size and larger than the mean free path of change carriers. The different coordination numbers (Z) correspond to different electron percolation thresholds. The measured electron percolation threshold for the composite is above 75 vol.% of CGO and agrees with the assumption of Z = 8. The extracted high coordination number is well in line with a very similar grain size distribution of the LSF and the CGO phases. The average grain sizes were 0.50 ± 0.26 μm for LSF and 0.55 ± 0.20 μm for CGO. This further indicates that for the random distribution of CGO and LSF phases a very small amount of the electron conductive phase is needed to ensure the electron percolation.

For the demand of the high conductivity at high pO_2 (air) the composition with 70 vol.% of CGO was selected for further studies to compromise between a high enough electronic conductivity, originating from the electron hole percolation in the LSF phase, and a high oxygen ion conductivity, originating from the CGO matrix. Figure 3b shows the electrical conductivity of the CGO-LSF (bar) (CGO:LSF = 70:30 vol.%) as a function of the oxygen activity ($a(O_2) = pO_2 / p_{tot}$) at different temperatures. At high $a(O_2)$ (> 10^{-5}) the change of the conductivity with $a(O_2)$ follows a power law ($\sigma \propto (a(O_2))^n$) with n = 0.1 – 0.2, which indicates a dominating *p*-type conductivity of the percolating LSF phase. At low $a(O_2)$ (< 10^{-12}) the exponent n is close to -¼ and indicates a dominating *n*-type conductivity. The electrical conductivity of the CGO-LSF composite at low $a(O_2)$ originates mostly from the CGO phase (due to reduction of Ce^{4+} to Ce^{3+}) and it is slightly reduced for the composite compared to pure CGO, as shown by Cheng et al.[21]. At intermediate $a(O_2)$ (between 10^{-9} – 10^{-10} at 900 °C) the electrical conductivity passes through a minimum, as expected from the properties of the two materials.

The *p*-type conductivity shows a different temperature dependence than the *n*-type. The *p*-type conductivity decreased with increasing temperature in the range 700 °C - 900 °C. The same was reported for pure LSF [10] and CGO-LSF[30] composites, where the conductivity increased until ca. 500 °C, went through a broad maximum at temperatures between 500 °C and 600 °C and then decreased with increased temperature above 600 °C. At low $a(O_2)$ the electrical conductivity of the composite increased with increasing temperature with an activation energy of 82 kJ/mol at pO_2 of 1.01325 x 10^{-13} Pa ($a(O_2) = 10^{-18}$) (Figure 3b).

To illustrate how the electronic conductivity dominates in the composite, the effective ionic conductivities at 750 °C and 900 °C of the composite are shown in Figure 3b for two cases: i) only CGO in the composite (CGO 70 vol.%) and ii) CGO and LSF in the composite (CGO:LSF = 70:30 vol%). The effective ionic conductivities were calculated from ionic conductivity of LSF [10] and CGO [13], weighted by their respective volume fraction. The ionic conductivity of both only CGO and the composite is 2-3 times lower than the minimum total electrical conductivity of the composite. This demonstrates that the oxygen transport through the membrane will be limited by the ionic conductivity contribution and possibly surface reactions, but not by electronic conductivity. Additionally, the small difference between the estimated effective ionic conductivities of the composite with only CGO and with CGO-LSF shows that the ionic conductivity of the membrane is dominated by the contribution from the CGO, especially at lower temperatures.

3.3 Oxide ion diffusion

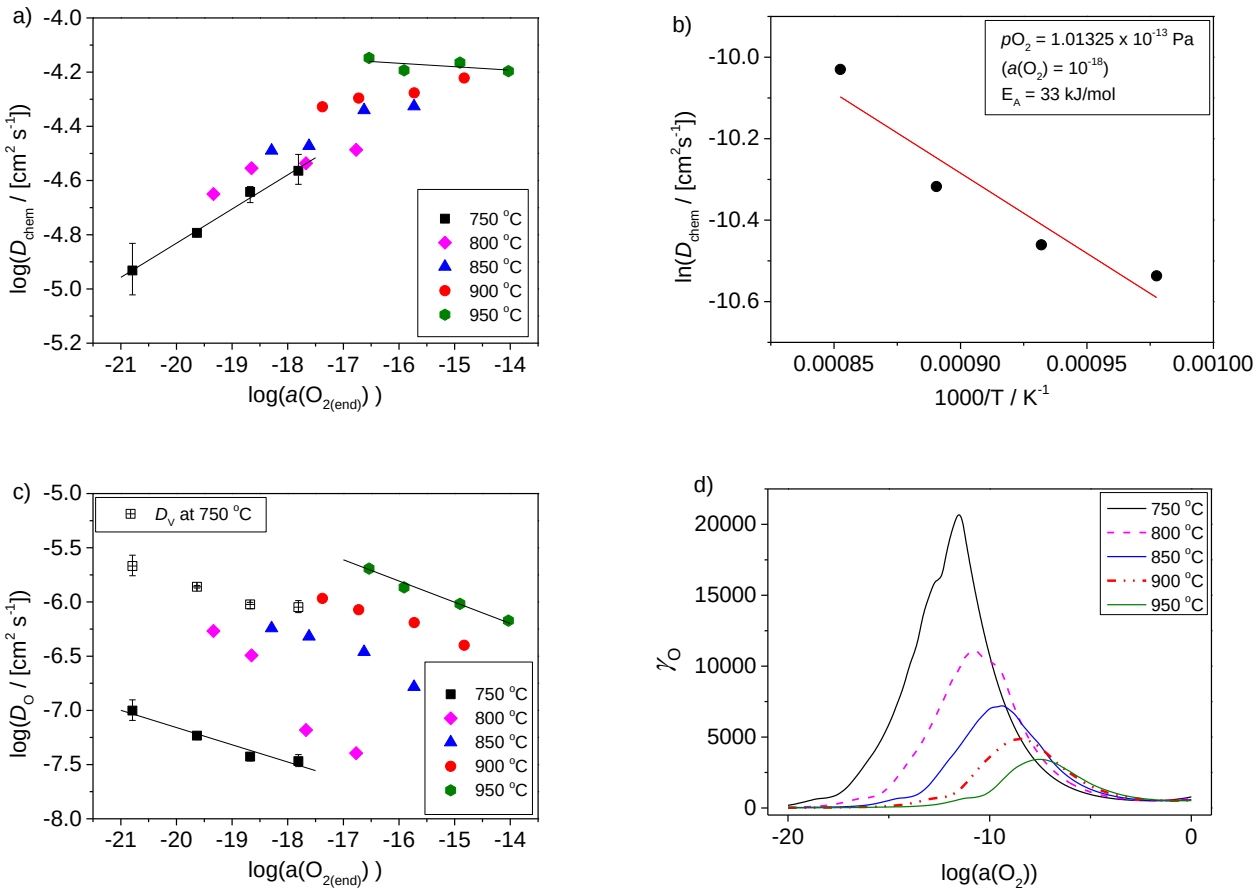

Figure 4: Temperature and oxygen activity dependence of a) chemical diffusion coefficient (D_{chem}), b) D_{chem} at $a(O_2) = 10^{-18}$, c) oxygen diffusion coefficient (D_O) and vacancy diffusion coefficient (D_V) for CGO-LSF (bar) deduced from the data in a) and the calculated thermodynamic factors γ_O d) at low pO_2.

The oxide ion transport properties were deduced from the transient response in conductivity to a step change in pO_2. Here, only D_{chem} values measured at low pO_2's as a function of end pO_2 ($a(O_{2(end)})$) are presented. The D_{chem} values at high pO_2 were reported in a previous study for a pO_2 range of $1.01325 \times 10^3 - 1.01325 \times 10^5$ Pa, where the reported D_{chem} was within $1.6 - 2.2 \times 10^{-4}$ cm^2/s with an activation energy of 100 kJ/mol [21]. Figure 4a shows the $a(O_2)$ dependence of D_{chem} in the temperature range 750 °C to 950 °C. At the oxygen activities below 10^{-17} the D_{chem} seems to decrease with decreasing $a(O_2)$ and at a temperature of 750 °C it follows $D_{chem} \propto a(O_2)^{0.1}$. However, one shall have in mind that at low temperatures the conductivity relaxation is governed by the surface exchange. Thus the accuracy in the measurement of D_{chem} decreases, as suggested by the larger error bars in Figure 4a, and the $a(O_2)$ dependence will therefore also be affected by increased uncertainty at low temperature.

In Figure 4b an Arrhenius plot of D_{chem} (for a pO_2 of 1.01325×10^{-13} Pa), where the values of D_{chem} were estimated from the $D_{chem} - a(O_2)$ dependence shown in Figure 4a, is presented. A D_{chem} of 4.4×10^{-5} cm^2/s at 900 °C with an activation energy of 33 kJ/mol was measured, which is in line with a reported D_{chem} of $3.3 \times 10^{-6} - 5.0 \times 10^{-5}$ cm^2/s for pure CGO measured under similar conditions [40].

Figure 4c shows the oxygen diffusion coefficient (D_O) and the vacancy diffusion coefficient (D_V) as a function of oxygen activity at different temperatures. The D_O and D_V were calculated from the measured D_{chem} using the estimated thermodynamic enhancement factors of the 70 vol.% CGO – 30 vol.% LSF composite (Eqs. 3), which are further illustrated in Figure 4d. A large uncertainty in the calculated D_O and D_V comes from determining the thermodynamic factor. Therefore, the D_O as well as D_V $a(O_2)$ dependance shown in Figure 4c can be incorrect and most probably D_O and D_V are constant or even slightly increasing with decreasing. The calculated ionic conductivity from D_v at 750 °C and $a(O_2)$ of 10^{-18} was 0.04 S cm^{-1} (see Figure 3b), which matches well with the estimated effective ionic conductivities of the composite. In other words, the values obtained from ECR are consistent with the values deduced from the conductivity measurements.

3.4 Surface exchange rate

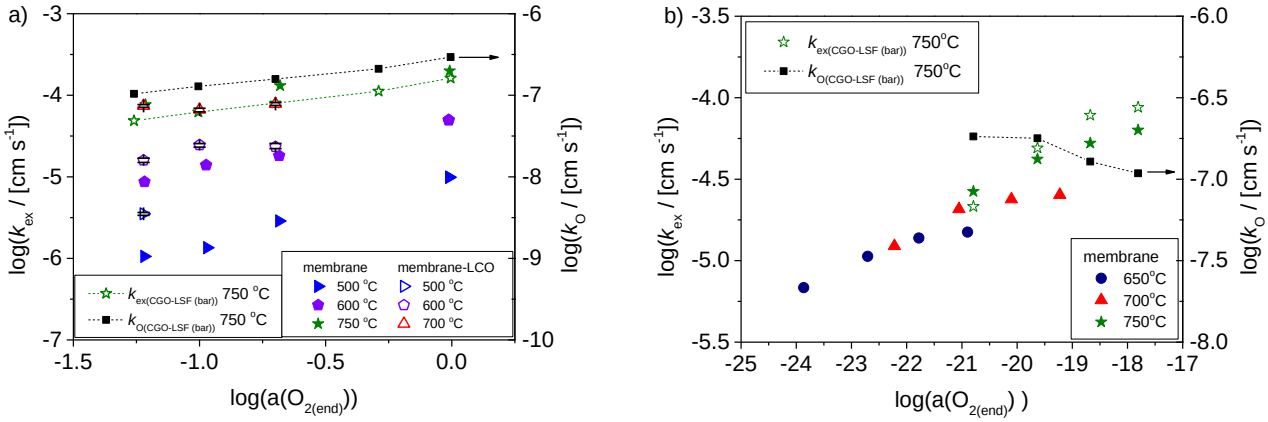

Figure 5: Surface exchange coefficient (k_{ex}) and oxygen surface exchange coefficient (k_O) as a function of $a(O_2)$ a) at high pO_2 for the CGO-LSF (bar), the membrane and the LCO infiltrated membrane and b) at low pO_2 for the membrane.

Figure 5a shows k_{ex} as a function of $a(O_2)$ in the high pO_2 range for three different samples, i) CGO-LSF (bar), ii) a piece of membrane, and iii) a piece of membrane infiltrated with LCO. The error bars (corresponding to SSD_{min} ± 5%) of the measured k_{ex} for the LCO infiltrated membrane obtained by fitting of Eq. 2 to the measured electrical conductivity relaxation curve are also presented in Figure 5a. The error of fitting is much smaller than the differences between the samples. The comparison between the samples was carried out only at low temperatures (500 – 750 °C), due to limitations of the measurement setup. At higher temperatures the conductivity relaxation was faster than the time needed to exchange the gas (t ~ 10 s). The $a(O_2)$ dependence of k_{ex} was the same for the membrane as for the CGO-LSF (bar) and can be described with $k_{ex} \alpha a(O_2)^{0.3}$. The same $a(O_2)$ dependence was reported by Cheng et al. [21] for a same composite, but k_{ex} deduced from pO_2 steps, where oxygen release was simulated (here the k_{ex} values were acquired by increased pO_2, see section 2.6). This indicates a good reproducibility and that the applied step changes are sufficiently small that the assumption of linear kinetics is warranted. The same pO_2 dependence was observed also for calculated k_O values at high pO_2. Comparing the k_{ex} values of different samples reveals that the k_{ex} of the membrane was slightly higher than that of the CGO-LSF (bar). An even higher k_{ex} was measured for the LCO infiltrated membrane. The enhancement of k_{ex} was due to the presence of the LCO catalyst on the surface of the dual-phase composite membrane. This is in agreement with the increased surface exchange of $La_{0.6}Sr_{0.4}Co_{0.8}Fe_{0.2}O_{3-d}$ coated with $Ce_{(1-x)}Sm_xO_{2-d}$ nanoparticles reported by Hong et al.[41], where the enhancement was correlated

with the fast reaction at the triple phase boundary (TPB). The infiltration of the LCO electron conductor into such a structure increases the TPB length and effectively accelerates the oxygen reduction reaction [42–44].

Figure 5b shows the a(O_2) dependence of k_{ex} for two different samples, i) a CGO-LSF (bar) and ii) a piece of membrane in the low pO_2 range. For both samples the measured k_{ex} values were similar and scaled with a(O_2)$^{0.1}$ at all temperatures. This indicates that the porous CGO layer by itself seems to have no beneficial effect on the surface exchange at low pO_2. However, the values of k_{ex} are in the same range as literature values for a pure CGO [40].

The a(O_2) dependence of k_O at 750 °C and low pO_2, calculated from the k_{ex} data and the thermodynamic factor shown in Figure 4d, is also shown in Figure 5b (symbol ■). The k_{ex} and k_O are strongly temperature dependent but effectively pO_2 independent.

3.5 Oxygen permeation rate of tubular asymmetric membrane

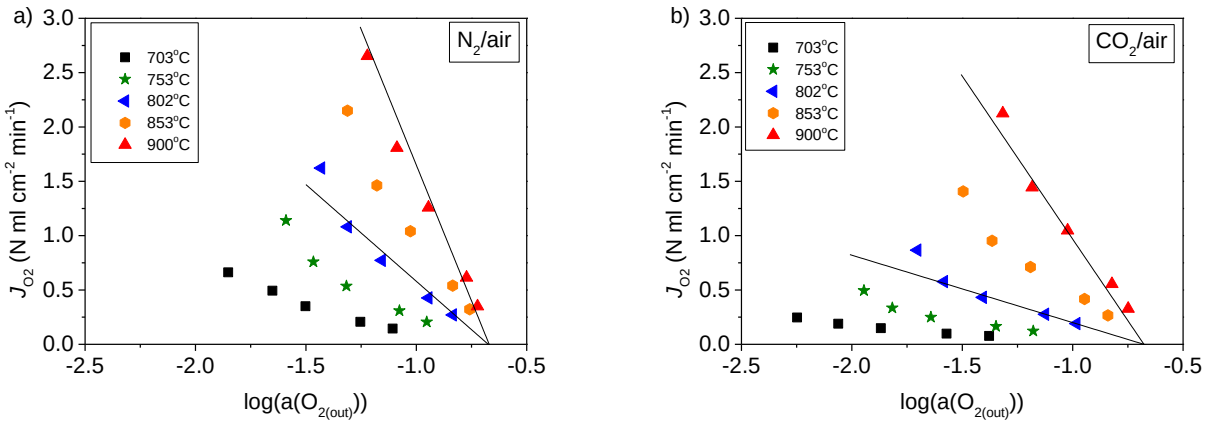

Figure 6: $J(O_2)$ as a function of a(O_2) for the 2.3 cm long tubular asymmetric CGO-LSF membrane at different temperatures with a) air as a feed gas and N_2 as a sweep gas (the N_2/air configuration), and b) air as a feed gas and CO_2 as a sweep gas (the for the CO_2/air configuration)

In Figures 6 the oxygen permeation flux at different temperatures and a($O_{2(out)}$) (the outlet oxygen activity), calculated as an outlet pO_2/p_{tot}, is shown. The oxygen activity at the feed side was 0.21. The $J(O_2)$ increases with increasing temperature and an increased pO_2 gradient for the presented configurations of gases (N_2/air, CO_2/air). The driving force of oxygen permeation through a membrane is the difference in the oxygen activity between the two sides of the membrane. For the both configurations within uncertainty the $J(O_2)$ extrapolates to 0 in the absence of driving force, when $\log(a(O_2)sweep/a(O_2)feed)=0$, which indicates the leak-less

setup with well calibrated mass flow controls. A lower $J(O_2)$ was observed for the CO_2/air configuration than for N_2/air configuration at the same temperature and pO_2 gradient (Figures 6a, 6b). In the CO_2/air configuration $J(O_2)$ shows different $a(O_{2(out)})$ dependence than in the N_2/air configuration and different temperature dependence. At 900 °C the $J(O_2)$ of the CO_2/air configuration was strongly activated and almost reached the measured $J(O_2)$ of the N_2/air. Furthermore, the activation energy of $J(O_2)$, calculated at fixed pO_2 gradient of 0.05/0.2, differs for these two configurations: 140 kJ/mol for the N_2/air configuration and 166 kJ/mol for the CO_2/air configuration.

The lower $J(O_2)$ measured in the CO_2/air configuration could be a consequence of the reaction between CO_2 and LSF at the operating temperature of the membrane and/or a CO_2 adsorption effect. It is expected that $SrCO_3$ formed on the surface of LSF will have no catalytic activity and will impede the surface exchange reaction. Evidence of formation of carbonates on the surface of the CGO-LSF composite membrane was reported by Cheng et al.[21]. Formation and decomposition of $SrCO_3$ is temperature dependent. At temperatures higher than 810 °C $SrCO_3$ starts to decompose and reaches the maximal rate of decomposition at 960 °C [14]. Therefore, it is anticipated that with increasing the operation temperature, the membrane's performance in CO_2 will gradually become comparable with the performance in N_2. This is indeed what is observed; the deviation in flux between the two configurations was decreased with increasing temperature. The difference in performance could also be due to preferential adsorption of CO_2 on the surface, which slows down the oxygen surface exchange reaction, as reported by Serra et al. [45].

A strong influence of the gas composition on the membrane performance at a constant pO_2 gradient points out that the membrane performance is mostly limited by the surface exchange reaction. Furthermore, a modification of the inner CGO porous layer can improve the surface exchange reaction by preventing formation of carbonates or even further by improving the intrinsic catalytic properties.

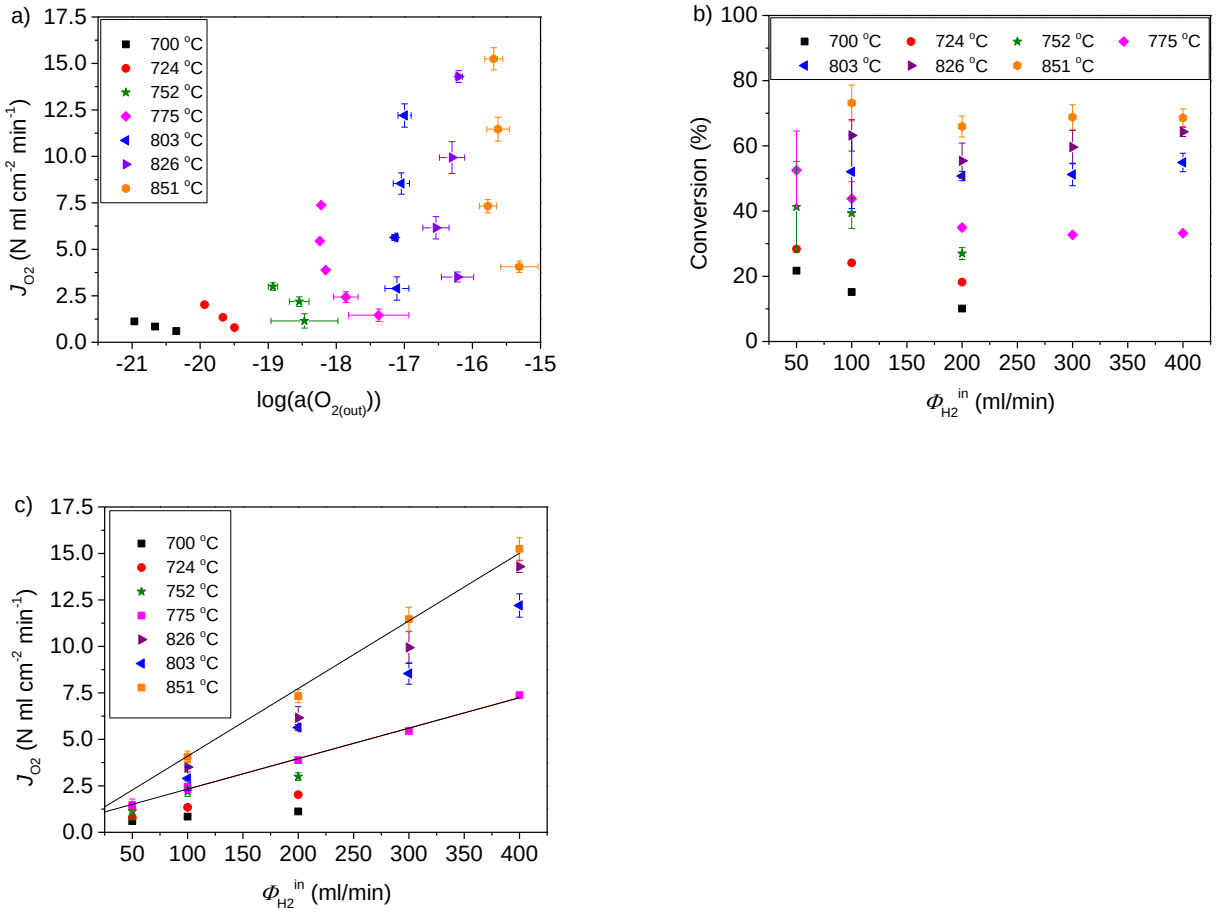

Figure 7: Performance of the 2.3 cm long tubular asymmetric CGO-LSF membrane with air as a feed gas and humidified H_2 as a reactive gas (the H_2/air configuration) at different temperatures: a) oxygen permeation flux ($J(O_2)$) as a function of a($O_{2(out)}$), b) conversion of H_2 as a function of the H_2 inlet flow rate (Φ_{H2}^{in}), and c) $J(O_2)$ as a function of Φ_{H2}^{in}

Figure 7 shows the performance of the 2.3 cm long tubular asymmetric CGO-LSF membrane in the H_2/air configuration, with air as a feed gas and H_2 as a reactive gas (this gas is taken as a model gas for the more technologically relevant case of a syngas mixture). A non-linear response of $J(O_2)$ on the outlet loga($O_{2(out)}$) especially at high temperature was observed (Figure 7a). At high temperature, the H_2 conversion rate to H_2O was large and did not depend on the H_2 flow rate, as shown in Figure 7b. The highest conversion rate of around 70 % was measured at 850 °C. A consequence of the high conversion rate is that the pO_2 gradient is significantly reduced along the membrane and the outlet pO_2 (a($O_{2(out)}$)) does not represent a local pO_2 inside the membrane. The deviation in the local pO_2 along the membrane is strongly increased with the increased

temperature. At high H_2 conversion, an additional error also originated from the setup limitations, where condensed water disturbs the pO_2 measurement. A fluctuation of the measured pO_2 values and the ensuing fluctuation in $J(O_2)$ is plotted in Figures 7 as error bars. In contrast to the $a(O_{2(out)})$ dependence, the $J(O_2)$ is linearly increasing with the H_2 inlet flow rate, as shown in Figure 7c. For the tested H_2 inlet flow rates no saturation of the membrane performance was observed. The highest flux of 15 N ml cm^{-2} min^{-1} was measured at 850 °C for the highest H_2 inlet flow rate of 400 ml/min.

3.6 Stability of the membrane

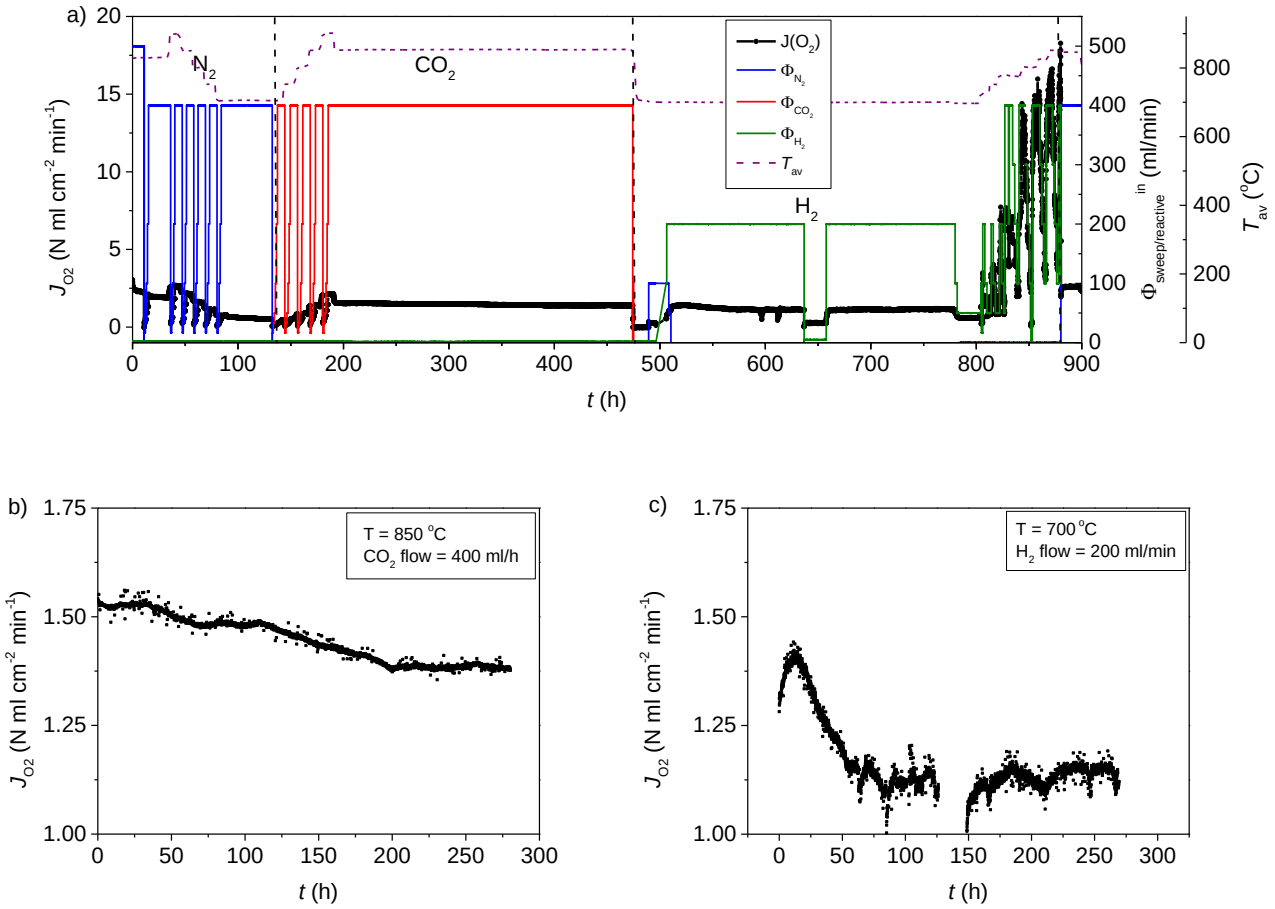

Figure 8: a) Test results for a 2.3 cm long tubular asymmetric CGO-LSF membrane. Stability tests with air as a feed gas and b) CO_2 as a sweep gas with flow rate of 400 ml/min at 850 °C, and c) humidified H_2 as a reactive gas with flow rate of 200 ml/min at 700 °C.

In Figure 8a the long-term performance test of the 2.3 cm long tubular asymmetric CGO-LSF membrane with air as a feed gas and different sweep gases or reactive H_2 gas at different temperature is shown. The total

testing time of the membrane was 900 h. Segments of the stability tests in the CO_2/air and H_2/air configurations are presented separately in Figures 8b and 8c, respectively. The stability performance tests were done on the same membrane as the other tests reported here in following sequence: i) the initial short tests in the N_2/air and CO_2/air configuration, results presented in Figure 6, ii) the stability test for 270 h in CO_2/air configuration at 850 °C, iii) the stability test in humidified H_2 (pO_2 ca. 10^{-16} Pa) /air configuration for 270 h at 700 °C, iv) the tests in the H_2/air configuration, results presented in Figures 7 and at last v) flushing the membrane with N_2. The stability test in CO_2/air shows that the performance was decreasing for the first 200 h and then it was relatively stable. However, the stability in remaining 70 h is too short for a final assessment and more elaborated test is needed. Similar behavior was also observed in H_2/air, where after the initial degradation (first 70 h of testing) the performance stabilized.

The oxygen permeation of the membrane at the end of the test, when the membrane was again flushed with N_2, was 2.5 N ml cm^{-2} min^{-1} at 850 °C and N_2 flow rate of 400 ml/min, which is slightly higher than at similar conditions at the beginning of the test (Figure 6a). However, unfortunately a comparison cannot be made due to presence of residual H_2 in the system, which resulted in a lower inlet a(O_2) of 10^{-14} (dead volume in a moisturizing bottle) in the post-testing period (t = 875 h) than at the start up (t = 25h).

Postmortem analysis of the tubular asymmetric CGO-LSF membrane did not reveal any significant microstructural change of the CGO-LSF dense membrane layer and the layer remained intact (Figure 2d). The cooling down of the membrane after testing below 500 °C resulted in peeling off of some parts of the membrane layer from the MgO porous support, which could be a consequence of re-oxidation of Ce^{3+} to Ce^{4+} and the extreme chemical contraction associated with it.

3.7 Comparison with theory

Figure 9a shows the calculated oxygen permeation flux through a thin dense CGO-LSF asymmetric dual-phase composite membrane supported on a porous MgO tube for the H_2/air configuration as a function of the activation polarization resistances (R_{surf}) of the surface exchange processes. The calculations were done according to the model reported by Chatzichristodoulou et al.[36] for two different temperatures of 750 °C and 900 °C, as is described in the section 2.8. R_{surf} was assumed to be the same on both sides of the membrane. Due to the fact that the ambipolar conductivity of the CGO-LSF membrane is rather insensitive on pO_2, it is the sum of the two R_{surf} that will determine the overall performance rather than its distribution between the two catalyst layers. Therefore, although unsubstantiated (but necessary in the absence of experimental values for each R_{surf}) this assumption is not expected to have a substantial influence on the outcome of the calculations.

The calculated oxygen permeation flux increases strongly with increasing performance of the catalyst (decreasing R_{surf}), as shown in Figure 9a. For an R_{surf} lower than 5 x 10^{-6} Ω m^2 the oxygen flux through the membrane reaches a saturation value as it becomes limited by gas diffusion through the MgO support. To exceed these values the microstructure of the MgO support must be modified. The maximal oxygen flux that can be achieved at 750 °C for flow of 400 Nml/min of H_2 through a 2.3 cm long membrane is approx. 17.0 N ml cm^{-2} min^{-1}. A slightly lower maximal flux of 16.8 N ml cm^{-2} min^{-1} was calculated for a temperature of 900 °C, due to the increased viscosity of gases.

The reader is reminded here that the ionic conductivity of LSF was assumed to be negligible in the calculations. The contribution of LSF to the total ionic conductivity would be approx. 8% at 750 °C and 29% at 900 °C. This is considered to be of a similar magnitude as other uncertainties that influence the effective ionic conductivity of the membrane, such as the variation in literature values for the ionic conductivity of CGO and LSF, possible inter-diffusion of cations between CGO and LSF, and micro-strain in the composite CGO-LSF membrane. Nevertheless, the accuracy of the effective ionic conductivity will only have a minor impact on the flux calculations, since the loss in driving force associated with ambipolar diffusion through the membrane is only a minor contribution to the overall losses, contributing with less than approx. 10% at 750 °C and 5% at 900 °C (see X_{trans} in Figure 9a). It should be stressed though that due to the lack of accurate experimental values for R_{surf} of each catalyst layer and of the effective ionic conductivity through the CGO-LSF membrane, the aim of the calculations is not to have a direct comparison with the experimental results, but rather to offer a semi-quantitative estimate of the expected O_2 flux, and more importantly to offer useful insight regarding the main processes that limit the overall performance.

In Figure 9a a breakdown of the driving force losses (X) to contributions of different processes is shown. The calculations predict that for the here studied tubular CGO-LSF asymmetrical membrane the major losses are due to the surface exchange losses (X_{ex}) and losses due to concentration polarization in the MgO support (X_{conc}). The contributions originating from the bulk transport losses (X_{trans}) and the conversion losses on the H_2 side (X_{conv}) have much smaller influence on the oxygen permeation flux. For the R_{surf} down to 4.5 x 10^{-6} Ω m^2 the calculations predict that the largest contribution to the driving force losses will come from the surface exchange losses (X_{ex}) and below this value the concentration polarization in the MgO support (X_{conc}) will start to dominate the oxygen permeation.

The surface exchange process is highly temperature dependent; a large decrease of R_{surf} with increased temperature occurs. Due to the fact that the calculated $J(O_2)$ dependence on R_{surf} values only slightly varies

with the temperature, the decrease of the membrane's R_{surf} can roughly be assessed from the calculated $J(O_2)$, shown in Figure 9a and the measured $J(O_2)$, shown in Figure 7. In essence it was assumed that the model accounts well for conversion losses, diffusion loss and bulk losses and the value of R_{surf} was used as a fitting parameter. The R_{surf} estimated in this way is at 750 °C 5.7 x 10^{-5} Ω m^2 and at 850 °C 7 x 10^{-6} Ω m^2 and the estimated activation energy of the surface exchange is 200 kJ/mol.

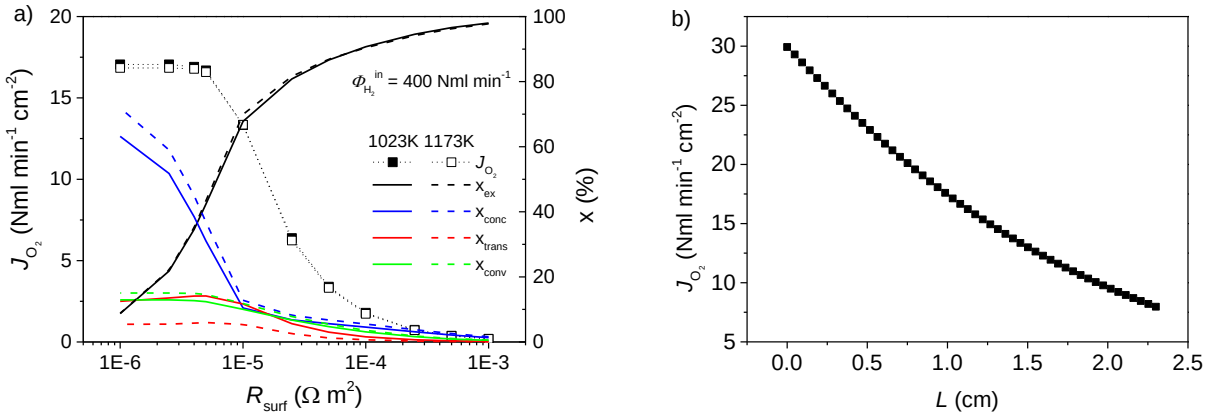

Figure 9: a) Oxygen permeation flux as a function of activation polarization resistances (R_{surf}) (J_{O2} is the calculated oxygen permeation flux, X_{ex}, X_{conc}, X_{trans} and X_{conv} are percentages of surface exchange losses, gas diffusion losses on the H_2 side, ohmic losses and conversion losses on the H_2 side, respectively), b) Calculated oxygen permeation flux along the length of the membrane (L) for an R_{surf} of 2.5 x 10^{-6} Ω m^2 at 750 °C.

Figure 9b shows the calculated oxygen permeation flux along the length of the membrane for an R_{surf} of 2.5 x 10^{-6} Ω m^2 at 750 °C. The average flux under these conditions was 17 N ml cm^{-2} min^{-1}. The oxygen permeation flux is decreasing along the length of the membrane, due to a decreased driving force as H_2 is gradually converted to H_2O. For the 2.3 cm long membrane and under the conditions chosen here, the calculations show that the oxygen flux at the outlet is decreased by a factor of 4 compared to the flux at the inlet.

By comparing the calculated and measured data it is evident that the oxygen transport through the membrane is limited by the surface exchange reaction. The R_{surf} calculated from k_{ex} at 750 °C of the CGO-LSF (bar) for high and low pO_2 was 1.8 x 10^{-3} Ω m^2 and 3.2 x 10^{-3} Ω m^2, respectively. The estimated R_{surf} from Figure 9a that corresponds to the measured $J(O_2)$ at 750 °C was 5.7 x 10^{-5} Ω m^2, several times smaller than expected from the surface exchange measurements at 750 °C. One reason for a lower R_{surf} than expected from the ECR deduced values of k_{ex} for the dense CGO-LSF (bar) is associated with the addition of the porous layers on both sides of the dense membrane layer and the infiltration of the outer one with a high oxygen partial pressure catalyst,

which increases the catalytic activity and the surface area where the oxygen reduction and oxidation occur. Thus, the surface exchange rate is increased. This was indeed observed by the high pO_2 ECR, where the infiltration of LCO into the CGO porous layer of the membrane increased the k_{ex}, by several times compared to k_{ex} for the membrane with the bare CGO porous layer or the bulk CGO-LSF (bar) (see Figure 5a), albeit this effect can only account for part of the improvement. Unfortunately, the relaxation data on the membrane piece with catalyst cannot be compared with the flux measurements on the membrane as the former can only be done up to 700 °C. At the low pO_2 no significant benefit of CGO porous layer compared to the dense CGO-LSF (bar) was observed by ECR. Another contribution to the deviation between the R_{surf} values (obtained from the ECR and the oxygen permeation flux measurements/modeling) can be ascribed to the different atmospheres used: the mixture of CO/CO_2 in the low pO_2 ECR and the humidified H_2 in the oxygen permeation.

The performance of the membrane can be influenced by catalysts, temperature, pO_2 gradient, etc. The introduction of a better catalyst and/or larger surface area in the CGO porous layer will increase the membrane performance significantly below 850 °C. However, for the here investigated membrane the predicted limiting factor at the highest oxygen flux in H_2/air configuration (at 850 °C) is in fact the microstructure of the MgO support and the associated gas diffusion resistance through it. The measured oxygen flux of 15 N ml cm^{-2} min^{-1} is most probably very close to the maximal one that can be achieved with this support structure of the membrane, as deduced from the modelling.

4 Conclusion

Oxygen transport membranes of dense $Ce_{0.9}Gd_{0.1}O_{1.95}$ – $(La_{0.6}Sr_{0.4})_{0.98}FeO_{3-d}$ (CGO-LSF) dual-phase composite supported on a porous MgO tube were prepared by thermoplastic extrusion, dip coating, co-sintering and infiltration with a catalyst. The membranes were tested, with respect to their oxygen permeation, conductivity and surface exchange in the temperature range of 500 – 900 °C and an oxygen partial pressure range of 2.0 x 10^4 Pa – 1.0 x 10^{-19} Pa. It was shown that the electronic conductivity is much higher than the ionic conductivity and that the oxygen transport through the membrane is for most of the tested configurations and temperatures controlled by the surface exchange. The oxygen flux for the N_2/air gradient and the H_2/air gradient at 850 °C reached 2.1 N ml cm^{-2} min^{-1} and 15 N ml cm^{-2} min^{-1}, respectively.

A model that takes into account the temperature and the pO_2 dependence of the bulk properties of the CGO-LSF composite, the activation polarization resistances (R_{surf}), the gas diffusion and the gas conversion was constructed and used to simulate the membrane performance. A comparison between theoretical and

experimental results was carried out for the H_2/air tests. Since the oxygen transport at lower temperatures was surface exchange limited, special focus was put on simulating the flux dependence of R_{surf}. As expected the results revealed that with decreasing R_{surf}, the oxygen flux can be largely increased. The R_{surf} can be reduced by increasing the operation temperature as R_{surf} is strongly temperature dependent, and/or by addition of a catalyst. For the membrane reported here the highest contribution to the R_{surf} most probably originates from low catalytic activity of the surface of the inner porous CGO layer, which should be improved in further studies in case of using the membranes at lower temperatures. However, the correlation between the measured and calculated flux revealed that for the highest investigated operation temperature 850 °C the oxygen flux almost reached the maximal theoretically predicted, diffusion through the MgO layer limited, flux of 17 N ml cm^{-2} min^{-1}. For further increasing the flux, the microstructure of the MgO porous support must be modified for higher gas permeability.

The stability tests of the membrane in CO_2/air and H_2/air configurations showed that after an initial degradation (up to 200 h) the performance of the membrane stabilized. The postmortem analysis of the tested membrane after 900 h of testing did not reveal any significant microstructural degradation in the membrane layer, but the adhesion of the membrane layer was significantly deteriorated during cooling below 500 °C.

The fair stability of the membrane as well as decent oxygen flux values show that this material system is promising for multipurpose membranes. This work lays out a clear direction for further improvements of the CGO-LSF membranes, which are an increase of the gas permeation in the support and the improvement of the catalytic activity on the inner membrane surface.

Acknowledgements

The authors acknowledge financial support from the ForskEL program of Energinet.dk through project 12202 “Ceramic Membranes for Oxy-Fired Biomass Gasification” and The Danish Council for Strategic Research though project Enefox – Energy efficient oxygen production for a sustainable energy system (DSF, 0603-00456B, 11-116387). The authors are also grateful towards Mrs. Ditte Lydia Vejlin Pedersen for help with experimental work on the electrical conductivity relaxation measurements. Dr. Philipp Zielke has contributed to this work with the careful revision of the English language.

References

[1] H.J.M. Bouwmeester, Dense ceramic membranes for methane conversion, Catal. Today. 82 (2003) 141–150. doi:10.1016/S0920-5861(03)00222-0.

[2] C. Delbos, G. Lebain, N. Richet, C. Bertail, Performances of tubular La08Sr0.2Fe0.7Ga0.3O3-delta mixed conducting membrane reactor for under pressure methane conversion to syngas, Catal. Today. 156 (2010) 146–152. doi:10.1016/j.cattod.2010.04.047.

[3] H.H. Wang, Y. Cong, W.S. Yang, Partial oxidation of ethane to syngas in an oxygen-permeable membrane reactor, J. Memb. Sci. 209 (2002) 143–152. doi:10.1016/S0376-7388(02)00323-X.

[4] J.P. Kim, E. Magnone, J.H. Park, Y. Lee, Oxygen production of tubular module with La0.6Sr0.4Ti0.3Fe0.7O3-delta coated Ba0.5Sr0.5Co0.8Fe0.2O3-delta membrane, J. Memb. Sci. 403 (2012) 188–195. doi:10.1016/j.memsci.2012.02.043.

[5] H.H. Wang, Y. Cong, W.S. Yang, Oxygen permeation study in a tubular Ba0.5Sr0.5Co0.8Fe0.2O3-delta oxygen permeable membrane, J. Memb. Sci. 210 (2002) 259–271. doi:10.1016/S0376-7388(02)00361-7.

[6] S. Baumann, J.M. Serra, M.P. Lobera, S. Escolástico, F. Schulze-Küppers, W.A. Meulenberg, Ultrahigh oxygen permeation flux through supported Ba0.5Sr0.5Co0.8Fe0.2O3−δ membranes, J. Memb. Sci. 377 (2011) 198–205. doi:10.1016/j.memsci.2011.04.050.

[7] S. Hashimoto, Y. Fukuda, M. Kuhn, K. Sato, K. Yashiro, J. Mizusaki, Oxygen nonstoichiometry and thermo-chemical stability of La0.6Sr0.4Co1-yFeyO3-δ (y=0.2, 0.4, 0.6, 0.8), Solid State Ionics. 181 (2010) 1713–1719. doi:10.1016/j.ssi.2010.09.024.

[8] W. He, H. Huang, M. Chen, J. Gao, C. Chen, Stability and oxygen transport property of La0.8Sr0.2Cr0.5Fe0.5O3-δ, Solid State Ionics. 260 (2014) 86–89. doi:10.1016/j.ssi.2014.03.018.

[9] A.J. Samson, M. Sogaard, P.V. Hendriksen, (Ce,Gd)O2-delta-based dual phase membranes for oxygen separation, J. Memb. Sci. 470 (2014) 178–188. doi:10.1016/j.memsci.2014.07.028.

[10] M. Sogaard, P.V. Hendriksen, M. Mogensen, Oxygen nonstoichiometry and transport properties of strontium substituted lanthanum ferrite, J. Solid State Chem. 180 (2007) 1489–1503. doi:10.1016/j.jssc.2007.02.012.

[11] B.T. Dalslet, M. Sogaard, H.J.M. Bouwmeester, P.V. Hendriksen, Defect chemistry and oxygen transport of (La0.6Sr0.4-xMx)(0.99)Co0.2Fe0.8O3-delta, M = Ca (x=0.05, 0.1), Ba (x=0.1, 0.2), Sr Part I: Defect chemistry, Solid State Ionics. 180 (2009) 1173–1182. doi:10.1016/j.ssi.2009.05.011.

[12] D. Chen, Z. Shao, Surface exchange and bulk diffusion properties of Ba0.5Sr0.5Co0.8Fe0.2O3−δ mixed conductor, Int. J. Hydrogen Energy. 36 (2011) 6948–6956. doi:10.1016/j.ijhydene.2011.02.087.

[13] S. Wang, T. Kobayashi, M. Dokiya, T. Hashimoto, Electrical and Ionic Conductivity of Gd-Doped Ceria, J. Electrochem. Soc. 147 (2000) 3606. doi:10.1149/1.1393946.

[14] S. Maitra, N. Chakrabarty, J. Pramanik, Decomposition kinetics of alkaline earth carbonates by integral approximation method, Cerâmica. 54 (2008) 268–272. doi:10.1590/S0366-69132008000300001.

[15] V. V. Kharton, F. Figueiredo, L. Navarro, E. Naumovich, A. Kovalevsky, A. Yaremchenko, A. Viskup, a Carneiro, F. Marques, J. Frade, Ceria-based materials for solid oxide fuel cells, J. Mater. Sci. 36 (2001) 1105–1117. doi:10.1023/A:1004817506146.

[16] M. Balaguer, C. Solís, J.M. Serra, Structural–Transport Properties Relationships on Ce 1– x Ln x O 2−δ System (Ln = Gd, La, Tb, Pr, Eu, Er, Yb, Nd) and Effect of Cobalt Addition, J. Phys. Chem. C. 116 (2012) 7975–7982. doi:10.1021/jp211594d.

[17] C. Chatzichristodoulou, P. V Hendriksen, Electronic conductivity of Ce0.9Gd0.1O1.95-delta and Ce0.8Pr0.2O2-delta: Hebb-Wagner polarisation in the case of redox active dopants and interference, Phys. Chem. Chem. Phys. 13 (2011) 21558–21572. doi:10.1039/c1cp21824g.

[18] C. Chatzichristodoulou, S. Ricote, S.P.V. Foghmoes, J. Glasscock, A. Kaiser, P.V. Hendriksen, Enhanced reducibility and electronic conductivity of Nb or W doped Ce0.9Gd0.1O1.95−δ, Solid State Ionics. 269 (2015) 51–56. doi:10.1016/j.ssi.2014.11.011.

[19] C. Chatzichristodoulou, M. Søgaard, J. a. Glasscock, A. Kaiser, S.P.V. Foghmoes, P.V. Hendriksen, Oxygen Permeation in Thin, Dense Ce0.9Gd0.1O1.95-delta Membranes II. Experimental Determination, J. Electrochem. Soc. 158 (2011) F73–F83. doi:10.1149/1.3559189.

[20] T.J. Mazanes, T.L. Cable, J.J. Frye, W.R. Kliewer, Novel solid multi-component membranes, electrochemical reactor and use of membranes and reator for oxidation reactions, US5306411 (A), 1994.

[21] S. Cheng, H. Huang, S. Ovtar, S.B. Simonsen, M. Chen, W. Zhang, M. Søgaard, A. Kaiser, P.V. Hendriksen, C. Chen, High-Performance Microchanneled Asymmetric Gd 0.1 Ce 0.9 O 1.95−δ –La 0.6 Sr 0.4 FeO 3−δ - Based Membranes for Oxygen Separation, ACS Appl. Mater. Interfaces. (2016) acsami.5b10714. doi:10.1021/acsami.5b10714.

[22] C. Gaudillere, J. Garcia-Fayos, M. Balaguer, J.M. Serra, Enhanced Oxygen Separation through Robust Freeze-Cast Bilayered Dual-Phase Membranes, ChemSusChem. 7 (2014) 2554–2561.

doi:10.1002/cssc.201402324.

[23] W. Fang, Y. Zhang, J. Gao, C. Chen, Oxygen permeability of asymmetric membrane of functional La0.8Sr0.2Cr0.5Fe0.5O3−δ(LSCrF)–Zr0.8Y0.2O2−δ(YSZ) supported on porous YSZ, Ceram. Int. 40 (2014) 799–803. doi:10.1016/j.ceramint.2013.06.070.

[24] C. Yang, Q. Xu, C. Liu, J. Liu, C. Chen, W. Liu, Bi1.5Y0.3Sm0.2O3–La0.8Sr0.2MnO3−δ dual-phase composite hollow fiber membrane for oxygen separation, Mater. Lett. 65 (2011) 3365–3367. doi:10.1016/j.matlet.2011.07.062.

[25] Q. Li, X. Zhu, W. Yang, Single-step fabrication of asymmetric dual-phase composite membranes for oxygen separation, J. Memb. Sci. 325 (2008) 11–15. doi:10.1016/j.memsci.2008.08.002.

[26] Z. Cao, X. Zhu, W. Li, B. Xu, L. Yang, W. Yang, Asymmetric dual-phase membranes prepared via tape-casting and co-lamination for oxygen permeation, Mater. Lett. 147 (2015) 88–91. doi:10.1016/j.matlet.2015.02.033.

[27] D.K. Ramachandran, K. Kwok, M. Søgaard, F. Clemens, A.J. Glasscock, A. Kaiser, The role of sacrificial fugitives in thermoplastic extrusion feedstocks on properties of MgO supports for oxygen transport membranes, J. Eur. Ceram. Soc. 35 (2015) 1527–1537. doi:10.1016/j.jeurceramsoc.2014.11.014.

[28] J. Gurauskis, S. Ovtar, A. Kaiser, M. Søgaard, P.V. Hendriksen, Ceria Based Composite Membranes for Oxygen Separation, ECS Trans. 64 (2014) 251–258. doi:10.1149/06402.0251ecst.

[29] A.J. Samson, M. Sogaard, N. Bonanos, Electrodes for Solid Oxide Fuel Cells Based on Infiltration of Co-Based Materials, Electrochem. Solid State Lett. 15 (2012) B54–B56. doi:10.1149/2.020204esl.

[30] S. Ovtar, M. Sogaard, P. V Hendriksen, K. Norrman, Enhancement of oxygen transport properties in (La0.6Sr0.4)0.98FeO3 and Ce0.9Gd0.1O1.95 dual-phase composites, Prep. (n.d.).

[31] M. Mosleh, M. Sogaard, P.V. Hendriksen, Kinetics and Mechanisms of Oxygen Surface Exchange on La0.6Sr0.4FeO3-delta Thin Films, J. Electrochem. Soc. 156 (2009) B441–B457. doi:10.1149/1.3062941.

[32] P. Hjalmarsson, M. Sogaard, M. Mogensen, Oxygen transport properties of dense and porous (La0.8Sr0.2)(0.99)Co0.8Ni0.2O3-delta, Solid State Ionics. 180 (2009) 1290–1297. doi:10.1016/j.ssi.2009.07.012.

[33] M. Sogaard, A. Bieberle-Huetter, P.V. Hendriksen, M. Mogensen, H.L. Tuller, Oxygen incorporation in

porous thin films of strontium doped lanthanum ferrite, J. Electroceramics. 27 (2011) 134–142. doi:10.1007/s10832-011-9658-3.

[34] S.R. Wang, H. Inaba, H. Tagawa, M. Dokiya, T. Hashimoto, Nonstoichiometry of Ce0. 9Gd0. 1O1. 95-x, Solid State Ionics. 107 (1998) 73–79. doi:10.1016/S0167-2738(97)00519-5.

[35] D.D. Wagman, J.E. Kilpatrick, W.J. Taylor, K.S. Pitzer, F.D. Rossini, Heats, free energies, and equilibrium constants of some reactions involving O2, H2, H2O, C, CO, CO2, and CH4, J. Res. Natl. Bur. Stand. (1934). 34 (1945) 143. doi:10.6028/jres.034.004.

[36] C. Chatzichristodoulou, M. Søgaard, P. V Hendriksen, Oxygen permeation in thin, dense Ce0.9Gd0.1O 1.95- membranes I. Model study, J. Electrochem. Soc. 158 (2011) F61–F72. doi:10.1149/1.3556096.

[37] Z. Wu, Modelling of ambipolar transport properties of composite mixed ionic-electronic conductors, Solid State Ionics. 93 (1996) 65–84. doi:10.1016/S0167-2738(96)00521-8.

[38] H.-C. Chang, G. Jaffé, Polarization in Electrolytic Solutions. Part I. Theory, J. Chem. Phys. 20 (1952) 1071. doi:10.1063/1.1700669.

[39] B. Dalslet, P. Blennow, P. V Hendriksen, N. Bonanos, D. Lybye, M. Mogensen, Assessment of doped ceria as electrolyte, J. Solid State Electrochem. 10 (2006) 547–561. doi:10.1007/s10008-006-0135-x.

[40] Y. Wang, Y. Wang, C. Xia, Surface Process of Doped Ceria Reduction by Electrical Conductivity Relaxation, J. Electrochem. Soc. 159 (2012) F570–F576. doi:10.1149/2.037209jes.

[41] T. Hong, L. Zhang, F. Chen, C. Xia, Oxygen surface exchange properties of La0.6Sr0.4Co0.8Fe0.2O3-(delta) coated with SmxCe1-O-x(2)-(delta), J. Power Sources. 218 (2012) 254–260. doi:10.1016/j.jpowsour.2012.07.004.

[42] Y. Wang, L. Zhang, C. Xia, Enhancing oxygen surface exchange coefficients of strontium-doped lanthanum manganates with electrolytes, Int. J. Hydrogen Energy. 37 (2012) 2182–2186. doi:10.1016/j.ijhydene.2011.11.008.

[43] Y. Ji, J.A. Kilner, M.F. Carolan, Electrical properties and oxygen diffusion in yttria-stabilised zirconia (YSZ)-La0.8Sr0.2MnO3 +/-delta (LSM) composites, Solid State Ionics. 176 (2005) 937–943. doi:10.1016/j.ssi.2004.11.019.

[44] S.P. Jiang, W. Wang, Fabrication and performance of GDC-impregnated (La,Sr)MnO3 cathodes for

intermediate temperature solid oxide fuel cells, J. Electrochem. Soc. 152 (2005) A1398–A1408. doi:10.1149/1.1928167.

[45] J.M. Serra, J. Garcia-Fayos, S. Baumann, F. Schulze-Küppers, W.A. Meulenberg, Oxygen permeation through tape-cast asymmetric all-La0.6Sr0.4Co0.2Fe0.8O3−δ membranes, J. Memb. Sci. 447 (2013) 297–305. doi:10.1016/j.memsci.2013.07.030.